

Improving Velocity Gradient Statistical Topology using Parameterized Lagrangian Attention Tensor Networks

Criston Hyett, Yifeng Tian, Michael Woodward, Misha Stepanov,
Chris Fryer, Daniel Livescu, Michael Chertkov

February 12, 2025

Abstract

We develop a Physics-Informed Neural Stochastic Ordinary Differential Equation-based closure model for the Velocity Gradient (VG) in isotropic homogeneous turbulence, extending the Tensor Basis Neural Network (TBNN) framework. Our new model, called the Lagrangian Attention Tensor Network (LATN), introduces a Neural Network-based parameterization for the unresolved terms in the Navier-Stokes equations for the VG. This parameterization is expressed as a nonlinear, auto-regressive and stochastic functional of the VG evaluated along a Lagrangian path. The “deformation” in the model’s name reflects a reference to the previously reported phenomenological closures, which utilize both the VG and the Lagrangian deformation tensor. Consequently, our model encapsulates both the TBNN and the phenomenological deformation approaches by incorporating the Lagrangian memory into. The Physics-Informed nature of the LATN model allows new insights into temporal correlations of the Lagrangian memory kernel and thus the strain-rate tensor’s history, and significantly improving predictions related to the pressure Hessian-VG relationship.

1 Introduction

The study of the Velocity Gradient Tensor (VGT), a classic and pivotal object in understanding turbulence, began with early closure attempts by Vieillefosse[47] and Cantwell[3], leading to significant insights through simulations [1] and experiments [45]. A key observation from this work was the statistically preferential alignment of the pressure Hessian with different components of the VGT – an idea central to the Vieillefosse-Cantwell closure model. However, it soon became evident that this closure, while stimulating further research, was fundamentally flawed, as it led to an unphysical finite-time singularity. To address this issue, Chertkov et.al[7] proposed a Lagrangian approach; resisting the singularity by utilizing a tetrad of tracer particles to track deformation along a Lagrangian trajectory. The motivations of the tetrad model were aligned with the progress in the late 1990s in understanding passive scalar and Burgers turbulence, as reviewed in [16]. The tetrad model successfully described the alignment of the pressure Hessian and VGT observed in experiments and simulations, building

a bridge to the classic study of energy cascades initiated by Kolmogorov in 1941 [25], and significantly advanced since [17].

However, the Lagrangian closure assumptions in [7] were difficult to verify directly in simulations, prompting the development of phenomenologies that avoided resolving spatial evolution of shapes. The new approaches suggested closures primarily in terms of local Lagrangian objects – specifically incorporating the so-called Recent Fluid Deformation (RFD) approximation [9]. See [31] for an overview of the RFD phenomenology and its connection to the earlier stochastic diffusion [18], linear damping [29], and linear diffusion [20] models. Development of the deformation tensor-based closure modeling of the pressure Hessian and viscous terms was also inspired by advances in Lagrangian simulations, particularly the challenging task of converting Eulerian Direct Numerical Simulation (DNS) data into Lagrangian data, as discussed in [51]. These datasets have enabled more in-depth study and closure modeling of the VGT, which is crucial for addressing unresolved problems in turbulence at high Reynolds numbers (Re), where DNS remains computationally unattainable. Such developments are important for improved sub-grid models in Large Eddy Simulations (LES) [40]. This combination of data availability at comparatively low Re , the need for closure models at high Re , and the conjectured universality of VGT statistics has inspired renewed interest in Lagrangian VGT modeling [12, 13, 23].

Throughout this development, the analysis of DNS datasets has played a crucial role in motivating and testing model hypotheses. This history of data-driven synthesis naturally aligns with advances in Machine Learning (ML). Specifically, Neural Network (NN)-based methods have emerged as powerful tools for analyzing Eulerian turbulence, as demonstrated by studies such as [28, 52, 24, 30, 15, 37, 32]. Approaching from the Lagrangian perspective, recent studies show the capability of physics-informed machine learning to model Lagrangian turbulence [43, 44, 53].

Some NN-based approaches to turbulence modeling, such as those in [52, 30, 15], have been predominantly data-driven, with physical symmetries, constraints, and interpretations incorporated retrospectively. In contrast, other methods, including those in [28, 37, 32, 43, 44, 53], were physics-informed in their structure. Both types of approaches align with the broader framework of Physics-Informed Machine Learning (PIML), which extends beyond turbulence applications – see [8] for a broader discussion of PIML and its importance in leveraging ML and AI to reveal the statistical nature of turbulence, complementing the classic pre-AI perspective [21].

Recent modeling efforts sought foremost to reproduce Lagrangian statistics [5, 14], while utilizing remaining freedom in the formulation to incorporate some physical properties. The impressive results of their by-construction reproduction of statistics of Lagrangian turbulence points to a new class of models to explore.

Our approach builds on the history of phenomenological Lagrangian models, utilizing the ideas of Lagrangian deformation incorporated via PIML to build an SDE around what we coin the Lagrangian Attention Tensor Network (LATN) model.

The rest of the manuscript is organized as follows: Section 2 presents background along with the two motivating approaches, Section 3 presents the LATN model and its connection to previous Lagrangian deformation approaches, with training and evaluation of the network in Section 4 and interpretations in Section 5.

2 Previous Work

2.1 Governing Equations for VGT

The incompressible Navier-Stokes equations in three dimensions, $\mathbf{x} = (x_i | i = 1, \dots, 3)$ define the evolution in time t of a velocity field $\mathbf{u}(\mathbf{x}, t) = (u_i(\mathbf{x}, t) | i = 1, \dots, 3)$

$$\frac{\partial u_i}{\partial t} + u_j \frac{\partial u_i}{\partial x_j} = -\frac{\partial p}{\partial x_i} + \nu \frac{\partial^2 u_i}{\partial x_j \partial x_j} + f_i, \quad (1)$$

where we use Einstein notations (summation over repeating indexes), the velocity is incompressible, $\partial_{x_i} v_i = 0$, and $\mathbf{f}(\mathbf{x}, t) = (f_i(\mathbf{x}, t) | i = 1, \dots, 3)$ is a large scale driving force of turbulence. Applying spatial derivatives to Eq. (1), using the definition of material derivative and ignoring the small scale component of the driving force, we obtain an ODE for the VGT $\mathbf{A}(\mathbf{x}, t) \doteq (A_{ij}(\mathbf{x}, t) = \frac{\partial u_i}{\partial x_j} | i, j = 1, \dots, 3)$:

$$\frac{dA_{ij}}{dt} = \frac{\partial A_{ij}}{\partial t} + u_k \frac{\partial A_{ij}}{\partial x_k} = -A_{ik} A_{kj} - \frac{\partial^2 p}{\partial x_i \partial x_j} + \nu \frac{\partial^2 A_{ij}}{\partial x_k \partial x_k}, \quad (2)$$

where transition from ∂_t to $d/dt = \partial_t + \mathbf{v} \nabla_{\mathbf{x}}$ emphasizes our interest in evaluation \mathbf{A} along the Lagrangian trajectories – that is in Lagrangian frame. Taking the trace of Eq. (2) and using the incompressibility condition, we re-write the evolution equation for the VGT in the Lagrangian frame as

$$\frac{dA_{ij}}{dt} = \underbrace{\left(\frac{1}{3} A_{kl} A_{lk} \delta_{ij} - A_{ik} A_{kj} \right)}_{E_{ij} \text{ (RE)}} + \underbrace{\left(\frac{1}{3} \frac{\partial p}{\partial x_k \partial x_k} \delta_{ij} - \frac{\partial^2 p}{\partial x_i \partial x_j} \right)}_{H_{ij} \text{ (PH)}} + \underbrace{\nu \frac{\partial^2 A_{ij}}{\partial x_k \partial x_k}}_{T_{ij} \text{ (VL)}}. \quad (3)$$

This equation has three traceless contributions: the purely local (not including spatial derivatives) ‘‘Restricted Euler’’ (RE) term, E_{ij} , the deviatoric, nonlocal Pressure Hessian (PH) term, H_{ij} , and the - also nonlocal - Viscous Laplacian (VL) term, T_{ij} .

2.2 Local Closures for the Evolution Equations

While the viscous term is dynamically important, historically effort was focused on modeling the deviatoric pressure Hessian as it directly resists the RE-induced finite time singularity [29, 43]. Therefore, in this section, we review the literature from the perspective of closing the Hessian term, and we will consider the viscous term separately (in Section 3.2).

2.2.1 Phenomenological Lagrangian Deformation Models

In the first attempt to locally close the VGT equations, the so-called Restricted Euler dynamics were studied:

$$\frac{dA_{ij}}{dt} \approx E_{ij} \quad (4)$$

and an asymptotic analysis found this reduction induced a finite-time singularity [48]. This was subsequently confirmed with specification of exact solutions, invariant dynamics and topological evolution under the RE dynamics [3, 4, 27].

The universal behavior of fluid elements induced by the purely local RE approximation was one motivation for the introduction of the Tetrad Model [7] that used four points to track and accumulate the history of the strain on a fluid element. This history was then utilized to close the nonlocal terms in Eq. (2), directly opposing the extreme flattening of the element and the acceleration of the phase plane dynamics along the Viellefosse tail. The RFD model was (in part) motivated by the tetrad model under a short-history approximation [9]. The RFD model - and subsequent models in this family - utilized the structure of the pressure Hessian and viscous Laplacian, preferring to specialize models for each nonlocal term rather than attempt to close the combination of the two as done in the tetrad model. Finally, along this line of postulation and enriching the upstream condition via fitting coefficients of a truncated tensor expansion - introduced originally by Pope [36] - the Recent Deformation of Gaussian Fields (RDGF) model was created [22] (the tensor expansion in question is treated in detail in Section 2.2.2).

Pervasive in this lineage is the idea that the deformation history of a fluid element can inform and improve Markovian models. To formalize this concept, we consider, following [9], the Lagrangian path map, $\mathbf{X} \in \mathbb{R}^3 \rightarrow \mathbf{x} \in \mathbb{R}^3$, which provides the Eulerian position \mathbf{x} at time t of a fluid particle that was initially at position \mathbf{X} at time t_0 . Due to incompressibility, this map is invertible, and its Jacobian, the deformation (gradient) tensor $\mathbf{D} = \left(D_{ij} = \partial x_i / \partial X_j \Big|_{i,j=1,\dots,3} \right)$, satisfies $\det(\mathbf{D}) = 1$ at all times. The time evolution of the deformation tensor is governed by the differential equation:

$$\frac{dD_{ij}}{dt} = A_{ik}D_{kj}, \quad \text{with } D_{ij}(0) = \delta_{ij}, \quad (5)$$

where \mathbf{A} represents the previously introduced VGT. The deformation tensor encapsulates the Lagrangian history of the fluid element and underpins many phenomenological history-based models, such as the Tetrad model [7], the RFD model [9], and the RDGF model [22]. As elaborated in Section 3, we draw upon this phenomenology to incorporate history terms into our data-driven framework.

2.2.2 Data-Driven Lagrangian Closures

We now return to the challenge of closing Eq. (3) through the approximation of the deviatoric Pressure Hessian (PH), H_{ij} , using data-driven methods. For incompressible turbulence, a formal nonlocal expression for the deviatoric pressure Hessian can be derived as an integral over the spatial domain [34]:

$$H_{ij}(\mathbf{x}) = \iiint \frac{\delta_{ij} - \bar{r}_i \bar{r}_j}{2\pi|\mathbf{r}|^3} Q(\mathbf{x} + \mathbf{r}) d\mathbf{r}, \quad (6)$$

where $Q = \frac{1}{2}A_{ij}A_{ji}$; $\mathbf{x}, \mathbf{r} \in \mathbb{R}^3$ and $\bar{\mathbf{r}} = \mathbf{r}/|\mathbf{r}|$. This representation highlights the non-local nature of the deviatoric pressure Hessian and its dependence on the surrounding VGT field.

It is well-established [36, 41] that any tensor-valued function $\mathbf{F} : \mathbb{R}^{3 \times 3} \rightarrow \mathbb{R}^{3 \times 3}$ of the VGT can be expressed as a Taylor series expansion over the strain rate and rotation rate tensors:

$$\mathbf{F}(\mathbf{A}) = \sum_{m,n=0}^{\infty} \alpha_{mn} \mathbf{S}^m \mathbf{W}^n,$$

where

$$S_{ij} = \frac{1}{2}(A_{ij} + A_{ji}), \quad W_{ij} = \frac{1}{2}(A_{ij} - A_{ji}),$$

are components of the symmetric strain rate tensor and the antisymmetric rotation rate tensor, respectively. This infinite series can be truncated into a finite sum using the Cayley-Hamilton theorem applied to \mathbf{A} . Further, if the tensor function $\mathbf{F}(\mathbf{A})$ is specified to be traceless, symmetric, and rotationally invariant, it can be represented using a tensor basis expansion [55]:

$$\mathbf{F}(\mathbf{A}) = \sum_{n=1}^{10} g^{(n)}(\lambda_1, \dots, \lambda_5) \mathbf{T}^{(n)}, \quad (7)$$

where $g^{(n)} : \mathbb{R}^5 \rightarrow \mathbb{R}$ are scalar functions of the five scalar invariants of the VGT:

$$\lambda_1 = \text{tr}(\mathbf{S}^2), \quad \lambda_2 = \text{tr}(\mathbf{W}^2), \quad \lambda_3 = \text{tr}(\mathbf{S}^3), \quad \lambda_4 = \text{tr}(\mathbf{W}^2 \mathbf{S}), \quad \lambda_5 = \text{tr}(\mathbf{W}^2 \mathbf{S}^2), \quad (8)$$

and the tensor basis $\{\mathbf{T}^{(n)}\}_{n=1}^{10}$ is composed of symmetric, traceless tensors:

$$\mathbf{T}^{(1)} = \mathbf{S}, \quad \mathbf{T}^{(2)} = \mathbf{S}\mathbf{W} - \mathbf{W}\mathbf{S}, \quad (9)$$

$$\mathbf{T}^{(3)} = \mathbf{S}^2 - \frac{1}{3}\mathbf{I} \cdot \text{tr}(\mathbf{S}^2), \quad \mathbf{T}^{(4)} = \mathbf{W}^2 - \frac{1}{3}\mathbf{I} \cdot \text{tr}(\mathbf{W}^2), \quad (10)$$

$$\mathbf{T}^{(5)} = \mathbf{W}\mathbf{S}^2 - \mathbf{S}^2\mathbf{W}, \quad \mathbf{T}^{(6)} = \mathbf{W}^2\mathbf{S} + \mathbf{S}\mathbf{W}^2 - \frac{2}{3}\mathbf{I} \cdot \text{tr}(\mathbf{S}\mathbf{W}^2), \quad (11)$$

$$\mathbf{T}^{(7)} = \mathbf{W}\mathbf{S}\mathbf{W}^2 - \mathbf{W}^2\mathbf{S}\mathbf{W}, \quad \mathbf{T}^{(8)} = \mathbf{S}\mathbf{W}\mathbf{S}^2 - \mathbf{S}^2\mathbf{W}\mathbf{S}, \quad (12)$$

$$\mathbf{T}^{(9)} = \mathbf{W}^2\mathbf{S}^2 + \mathbf{S}^2\mathbf{W}^2 - \frac{2}{3}\mathbf{I} \cdot \text{tr}(\mathbf{S}^2\mathbf{W}^2), \quad \mathbf{T}^{(10)} = \mathbf{W}\mathbf{S}^2\mathbf{W}^2 - \mathbf{W}^2\mathbf{S}^2\mathbf{W}. \quad (13)$$

Applying Eqs. (6,7) to the PH $\mathbf{H} \doteq \mathbf{F}(\mathbf{A})$ we arrive at:

$$\mathbf{H}_{ij}(\mathbf{x}) = \iiint \frac{\delta_{ij} - \bar{r}_i \bar{r}_j}{2\pi|\mathbf{r}|^3} Q(\mathbf{x} + \mathbf{r}) d\mathbf{r} \approx \sum_{n=1}^{10} g^{(n)}(\lambda_1, \dots, \lambda_5) T_{ij}^{(n)}. \quad (14)$$

Here, the spatial dependence of the pressure Hessian is implicitly captured through the VGT, i.e., there is an implicit dependence on \mathbf{x} via \mathbf{A} on the right-hand side of Eq. (14). Specifically, from Eqs. (8)–(13), the dependence on the VGT is evident: $\lambda_k = \lambda_k(\mathbf{A})$ and $\mathbf{T}^{(n)} = \mathbf{T}^{(n)}(\mathbf{A})$. For simplicity, this dependency is omitted from the notation.

This approximation reduces the nonlocal integration in Eq. (6) to the task of approximating the (potentially complex) scalar functions $g^{(n)}$ of locally known invariants. However, this relies on the *strong* assumption that the nonlocal contributions of Q can be effectively captured through observations of the local VGT. Supporting this expansion, numerical studies of the nonlocal integral in Eq. (6) suggest that, for extreme values of the VGT – regions in phase space that exert the strongest influence on the pressure Hessian terms – there is a shielding effect akin to that observed in electromagnetism. This shielding significantly reduces the effective integration scale in Eq. (6), as demonstrated in [49].

Due to the spatial locality of the approximation in Eq. (14), this formulation is particularly attractive for closure modeling of the VGT. Early models based on this approach analyzed DNS data to extract constant values of $g^{(n)}$, further assuming a

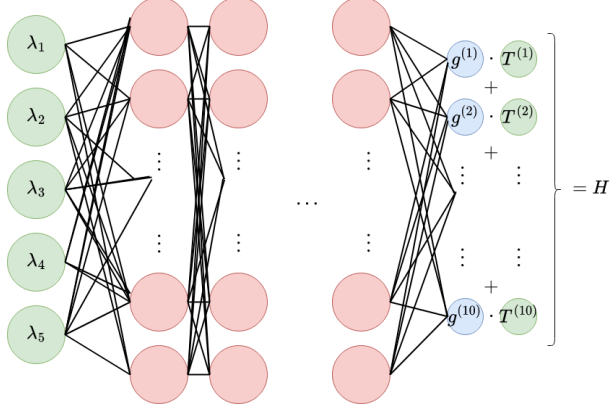


Figure 1: The architecture of the Tensor Basis Neural Network (TBNN). The invariants and tensor basis elements are calculated from each sample of the VGT, the invariants are then used as input to a fully connected network, and the resulting $g^{(i)}$ multiply the corresponding tensor basis elements $T^{(i)}$, before summing into the prediction $\hat{\mathbf{H}}$. The color scheme is the same as in Fig (2).

truncated tensor basis expansion [26]. This method is conceptually similar to the enrichment of the isotropic upstream condition used in the RDGF model, albeit with different underlying datasets – DNS for [26] and a Gaussian field for [22].

Subsequent advancements in [43] – coined Tensor Basis Neural Network (TBNN) – extended the VGT modeling approaches by utilizing the full tensor basis and allowing the $g^{(n)}$ functions to vary nontrivially as functions of the invariants. These functions were approximated in [43] using Neural Networks (NN), as illustrated in Fig. (1). This formulation led to the following minimization problem over θ -parameterized NN

$$\min_{\theta} \sum_{s=1}^S \|\mathbf{H}_s - \hat{\mathbf{H}}_s\|_2^2, \quad \text{where} \quad \hat{\mathbf{H}}_s = \sum_{n=1}^{10} g_{\theta}^{(n)}(\lambda_1, \dots, \lambda_5) \mathbf{T}^{(n)}. \quad (15)$$

Here, s runs over S samples, and $\mathbf{H}_s, \hat{\mathbf{H}}_s$ are the ground truth and predicted pressure Hessian for the s -th sample, respectively. An important feature of this formulation is that, regardless of the specific model used for $g_{\theta}^{(n)}$, the tensor basis structure ensures that the predicted tensor $\hat{\mathbf{H}}$ is symmetric, traceless, and rotationally invariant.

The results of [43] demonstrated that the expressive NN representation of $g^{(n)}$ trained effectively and delivered accurate predictions. State-of-the-art performance was achieved across various relevant physical metrics, including eigenvector alignments, Q - R conditional mean tangents (CMTs), and *a posteriori* tests, where an initially Gaussian fields evolve into fully turbulent ones with markedly non-Gaussian statistics. The characteristic teardrop-shaped Q - R probability distributions (PDFs) served as evidence of the model’s ability to capture key turbulence dynamics.

Following the marked success of the TBNN, subsequent work extended the formulation to enable generalization across Reynolds numbers [2]. Additionally, [35] highlighted the sensitivity of the TBNN architecture to the choice of normalization. For structural and physical consistency, we adopt the physics-inspired normalization scheme proposed in [43], which is detailed below.

3 Methodology of LATN

To motivate the Lagrangian Attention Tensor Network (LATN), observe the reduction in information present in the local-in-time approximation, central to the TBNN, Eq. (14). We hypothesize that the reduction from a nonlocal integral to a purely local expansion induces degeneracy – i.e. that there are similar values of the VGT with very different corresponding PH terms.

Motivated by previous phenomenological models utilizing the deformation tensor, we propose a data-driven, auto-regressive framework for conditional deviatoric PH prediction. Put simply, we directly generalize the TBNN, and enrich the lineage of VGT models by biasing predictions using prehistory:

$$\langle \mathbf{H}(t) | \mathbf{A}(t) \rangle \rightarrow \langle \mathbf{H}(t) | \mathbf{A}(t), \mathbf{A}(t - \Delta), \dots, \mathbf{A}(t - M\Delta) \rangle.$$

In the remainder of this section, we first describe, in Subsection 3.1, how time-delay – absent in TBNN – is incorporated into the LATN framework. Next, in Subsection 3.2, we discuss the motivation and methodology for applying this approach to model viscous losses. Finally, in Subsection 3.3, we complete the description of the model by providing details on how the ground truth data is utilized to train it.

3.1 Time-Delay Convolution for Pressure Hessian

Motivated by the deformation tensor considerations, i.e., the formal solution to Eq. (5),

$$\mathbf{D}(t; \mathbf{A}(t \leftarrow t - \tau)) = \text{Texp} \left(\int_{t-\tau}^t dt' \mathbf{A}(t') \right) = \lim_{M \rightarrow \infty} \prod_{m=0}^M \exp(\Delta \mathbf{A}(t_m)), \quad (16)$$

where $\Delta = \tau/M$, $t_m = t - m\Delta$, and Texp denotes the time-ordered exponential, we introduce a parameterizable approximation. First, note that each term on the right-hand side of Eq. (16) can be expanded as:

$$e^{\mathbf{A}(t_m)\Delta} = \sum_{p=0}^{\infty} \frac{(\mathbf{A}(t_m)\Delta)^p}{p!} = \mathbf{I} + \mathbf{A}(t_m)\Delta + \mathcal{O}(\Delta^2).$$

Fixing $\Delta \ll 1$ and taking the leading-order approximation in Δ , we obtain a first-order approximation for the deformation tensor:

$$\hat{\mathbf{D}}(t; \mathbf{A}(t \leftarrow t - \tau)) = \mathbf{I} + \Delta \sum_{m=0}^M \mathbf{A}(t_m) + \mathcal{O}(\Delta^2). \quad (17)$$

A plausible extension of the TBNN approach [43] to account for Lagrangian memory could involve directly incorporating the deformation tensor from Eq. (17) – considered as a specific function of $\mathbf{A}(t \leftarrow t - \tau)$ – into Eqs. (14, 15). However, we adopt a more general and flexible approach, enabling the model to adaptively forget history while emphasizing structural correlations within the VGT. Instead of working with the deformation tensor, we generalize and use functions of $\mathbf{A}(t \leftarrow t - \tau)$, represented through Time-Delay Neural Networks (TDNN) [50] – commonly referred to today as

Convolutional Neural Networks (CNN)—where the convolution is performed across time:

$$c^{(\ell)}\left(\mathbf{A}^{(0)}, \dots, \mathbf{A}^{(M)}\right) = \sigma\left(K_{ij}^{(m,\ell)} A_{ij}^{(m)}\right) \quad (18)$$

Here in Eq. (18), $c^{(\ell)}(\dots)$ represents the ℓ -th “temporal characteristic” (or, in CNN terminology, the alignment to the ℓ -th temporal convolution filter); $\sigma(\cdot)$ is a bounded activation function (we use $\sigma(\cdot) = \tanh(\cdot)$); $A_{ij}^{(m)} \doteq A_{ij}(t_m)$; and $K_{ij}^{(m,\ell)}$ are learnable weights. Note for fixed ℓ , $K_{ij}^{(m,\ell)} A_{ij}^{(m)}$ is a full tensor contraction, yielding a scalar.

These $c^{(\ell)}(\dots)$, which encode information about the temporal history of the VGT, are incorporated into the feed-forward portion of the TBNN, extending and generalizing Eq. (14):

$$\hat{\mathbf{H}} = \sum_{n=1}^{10} g_{\theta}^{(n)}(\lambda_1, \dots, \lambda_5, c^{(1)}, \dots, c^{(L)}) \mathbf{T}^{(n)}, \quad (19)$$

where the weights $K_{ij}^{(m,\ell)}$ are learned alongside the parameterization of the scalar g -functions. For clarity, we simplify the notation by omitting the explicit dependence on $\mathbf{A}(t \leftarrow t - \tau)$. This architecture is illustrated in Fig. (2). Two key deviations in the use of $c^{(\ell)}$ instead of D in Eq. (19) should be clarified: the use of a nonlinear activation, and a full tensor contraction.

The role of the nonlinear activation $\sigma(\cdot)$ is to bound $c^{(\ell)}$ for arbitrary samples of the VGT history, thereby providing stability to the feed-forward (FF) portion of the NN. The full tensor contraction reduces the risk of overtraining in the highly expressive FF network. Additionally, we intentionally omit the constant \mathbf{I} and the Δ multiplier in the transition from Eq. (17) to $c^{(\ell)}$ to avoid numerical issues for small Δ .

Formally, this formulation sacrifices rotational invariance, as the weights $K_{ij}^{(m,\ell)}$ can potentially align with specific rotations. Rotational invariance here refers to how $\hat{\mathbf{H}}(t)$ transforms under a consistent rotation of all $\mathbf{A}(t \leftarrow t - \tau)$ by the same angle. However, given the large rotationally invariant dataset and the relatively small number of additional learnable weights $K_{ij}^{(m,\ell)}$, we expect the rotational invariance of the data to prevent the network from specializing in any particular frame. This risk of overtraining can be further mitigated by tuning the hyperparameter L , which denotes the number of unique convolution filters.

We justify the full freedom of the convolutional kernels, rather than simply convolving a time-history of the invariants, to allow the network to capture correlations in the eigen-frame of the VGT. This design choice is motivated by the observed time-delayed alignment of vorticity and strain-rate [54].

The formulation in Eq. (18) shares similarities with classic work in TDNNs and CNNs [50]. However, our approach is motivated as a conceptual midpoint between the phenomenology of the deformation tensor and recent advances in transformer architectures, particularly the concept of attention [46]. While we avoid full multi-head attention due to concerns about interpretability, we see promise in generalizing the presented methodology to state-of-the-art transformers.

In summary, the LATN model (illustrated in Fig. (2)) accounts for historical information while avoiding the imposition of a specific phenomenological theory of historical importance. Moreover, due to the simple structure of the memory kernels, the learned temporal weights may be interpreted as temporal correlations in the VGT that are useful in predicting not only the PH term but also the VL term in Eq. (3). An extreme

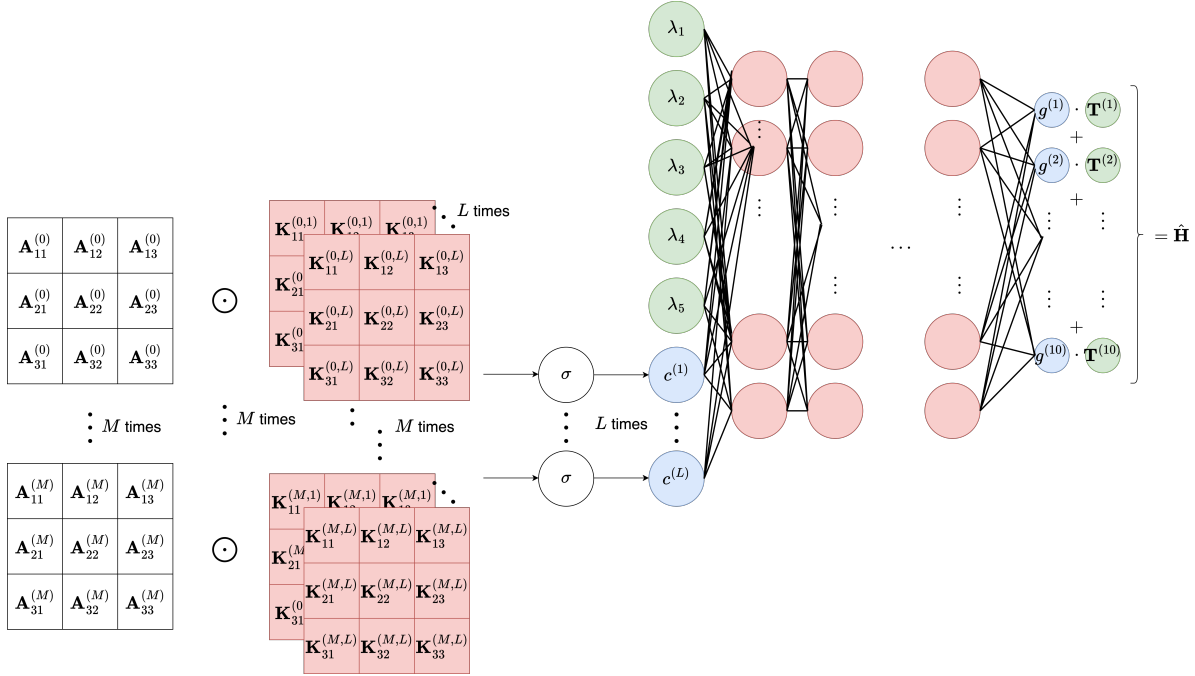


Figure 2: The full LATN; on the left the augmentation of temporal convolution feeding into the otherwise unchanged TBNN on the right, biasing the conditional statistics of $g_{\theta}^{(n)}(\lambda_1, \dots, \lambda_5, c^{(1)}, \dots, c^{(L)})$. The figure is color coded with: (white) information known before any processing occurs, (green) quantities that are directly calculable from a sample of the VGT, (red) parameters that are trained, and (blue) intermediate values calculated given a sample of the VGT and a set of parameters.

case of very short time correlations would reinforce the assumptions of RFD/RDGF, while longer temporal correlations would support richer memory approaches, such as those suggested in Mori-Zwanzig formulations [42].

3.2 Extension to the Viscous Laplacian Term

In this subsection, we extend the approach described in the previous subsection (applied to the Pressure Hessian (PH) term) to the modeling of the Viscous Laplacian (VL) term. For the TBNN, this involves augmenting the tensor basis defined in Eqs. (9-13) with additional skew-symmetric basis elements:

$$\mathbf{T}^{(11)} = \mathbf{W}, \quad \mathbf{T}^{(12)} = \mathbf{S}\mathbf{W} + \mathbf{W}\mathbf{S}, \quad (20)$$

$$\mathbf{T}^{(13)} = \mathbf{S}^2\mathbf{W} + \mathbf{W}\mathbf{S}^2, \quad \mathbf{T}^{(14)} = \mathbf{W}^2\mathbf{S} - \mathbf{S}\mathbf{W}^2, \quad (21)$$

$$\mathbf{T}^{(15)} = \mathbf{W}^2\mathbf{S}^2 - \mathbf{S}^2\mathbf{W}^2, \quad \mathbf{T}^{(16)} = \mathbf{S}\mathbf{W}^2\mathbf{S}^2 - \mathbf{S}^2\mathbf{W}^2\mathbf{S}. \quad (22)$$

We will build upon this extension, but first, we expand on a few subtle aspects of VL modeling.

First, in the original TBNN work [43], it was observed that naive application of the TBNN framework to the VL term using the L_2 norm often led to overfitting, which subsequently caused stiff dynamics in the resulting stochastic differential equation (SDE).

This issue was addressed by simplifying the network structure—reducing the fully nonlinear multilayer perceptron (MLP) architecture shown in Fig. (2) to a simple linear model, thereby preventing over-specialization.

Second, a topological perspective on viscous effects [12] highlighted the dynamically nontrivial and distinct role of the VL term in the statistical evolution of the VGT topology. This insight reinforces the importance of appropriately modeling the VL term to capture its unique contributions to phase-space dynamics.

Taking these observations into account, we propose using a nonlinear NN for the VL model to better capture its nontrivial effects while carefully addressing the potential for overfitting and the associated stiff dynamics. In Section 4, we demonstrate that the learned temporal kernels for the PH and VL networks exhibit distinct properties, highlighting the importance of separating these two parameterized models.

3.3 Ground Truth Data & Training

Our primary dataset is derived from Direct Numerical Simulation (DNS) of forced isotropic turbulence, governed by the NS equations (1), on an Eulerian grid with $Re \approx 240$. Using the Eulerian velocity field, we evolve Lagrangian tracer particles initialized at random locations. This provides 122,000 samples of single-particle trajectories, each advanced for 1000 timesteps with $\Delta t = 3 \times 10^{-4}$, representing approximately one inertial eddy turnover time. During these particle evolutions, we record the Velocity Gradient Tensor (VGT), Pressure Hessian (PH), and Viscous Laplacian (VL) contributions.

Given the sensitivity of the TBNN’s properties and training outcomes to normalization, as documented in the literature [35], we follow [43] in normalizing the VGT (and consequently the invariants and tensor basis) using the empirical Kolmogorov timescale:

$$\tau_K = \frac{1}{\langle \|S_{ij}\|_2^2 \rangle}.$$

As a side remark, recent studies [19] suggest that normalization itself may serve as an additional hyperparameter for optimization. In the feed-forward portion of the LATN, we adopt a simple Multi-Layer Perceptron (MLP) architecture as in [43], refined through hyperparameter search.

Two networks (one for each PH and VL), are trained in two stages. The first stage we term “tangent-space” optimization, contrasted with NeuralODE training detailed below. In tangent-space learning, we aggregate trajectories of duration τ , and minimize the L_2 error between the ground truth and predicted PH and VL at the final timestep in each series. This yields the optimization problem:

$$\theta_{PH} = \arg \min_{\theta} \sum_s \left\| \mathbf{H}_s - \hat{\mathbf{H}}_s \right\|_2^2, \quad \theta_{VL} = \arg \min_{\theta} \sum_s \left\| \mathbf{T}_s - \hat{\mathbf{T}}_s \right\|_2^2.$$

After this tangent-space optimization, we evaluate single-time predictions $\hat{\mathbf{H}}_{\theta_{PH}}$ and $\hat{\mathbf{T}}_{\theta_{VL}}$ through *a-priori* tests. With these predictions, we construct the parameterized Stochastic Differential Equation (SDE):

$$d\hat{\mathbf{A}} = \left(\mathbf{E} + \hat{\mathbf{H}}_{\theta_{PH}} + \hat{\mathbf{T}}_{\theta_{VL}} \right) dt + \hat{\mathbf{F}}(D_s, D_a) dW, \quad (23)$$

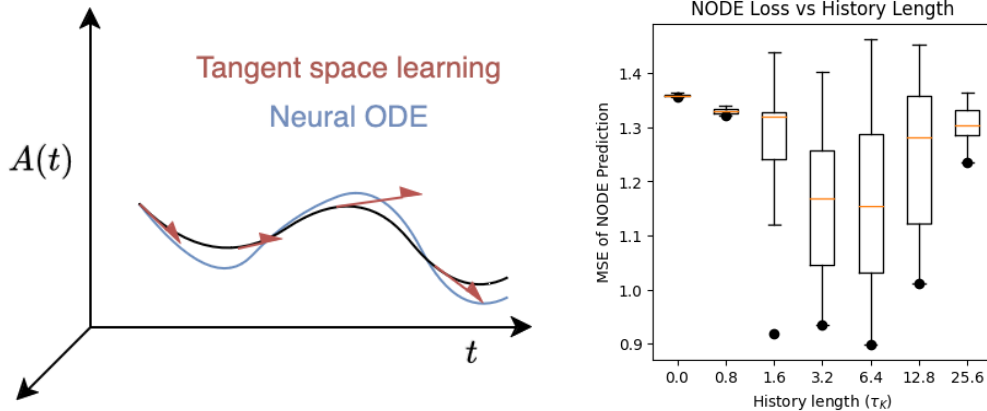


Figure 3: Schematic of Neural ODE vs tangent learning. Tangent learning is amenable to direct targeting of individual contributions (PH, VL) and priori interpretations; whereas utilizing the Neural ODE approach teaches the networks to work together to predict stable and dynamically relevant samples of the full VGT timeseries. We blend the two for priori interpretability and posteriori stability.

where $\hat{\mathbf{F}}(D_s, D_a)dW$ is an isotropic, traceless white noise process as described in [22].

To address the increased sensitivity of the LATN (arising from its potentially long memory), we further train the NNs within a Neural ODE framework [6]. This adjustment allows the PH and VL NNs to collaborate effectively, using their own outputs as inputs to build a coherent time-series. Fig. (3) illustrates the difference between tangent-space and Neural ODE training. Empirically, we find this additional training stabilizes predicted trajectories with minimal additional computational cost. One key hyperparameter is the length of the training rollout; we found that one Kolmogorov timescale, τ_K , is sufficient, as longer rollouts tend to make the network overly conservative due to the chaotic nature of turbulence.

Finally, fixing the parameter families θ_{PH} and θ_{VL} , we optimize the stochastic forcing parameters D_s and D_a by minimizing the residual after evolving the parameterized SDE over one Kolmogorov timescale:

$$D_s, D_a = \arg \min_{D_s, D_a} \left\langle \left\| \hat{\mathbf{A}}(\tau_K) - \mathbf{A}(\tau_K) \right\|_2^2 \middle| \mathbf{A}(0) \right\rangle. \quad (24)$$

4 Numerical Experiments

To evaluate the performance of the model, we rely on *a-priori* and *a-posteriori* metrics – that is, metrics for predictions at a single timestep and over multiple timesteps, respectively.

The *a-priori* metrics include test loss and probability density functions (PDFs) of eigenvector alignment. Test loss provides a coarse measure of tangent-space success under the L_2 norm, while eigenvector alignment PDFs illustrate the distribution of performance, offering insight into sample-level metrics.

The *a-posteriori* tests assess joint statistics after evolving Eq. (23) over a large eddy turnover time ($100\tau_K$), starting from DNS initial conditions. Historically *posteriori*

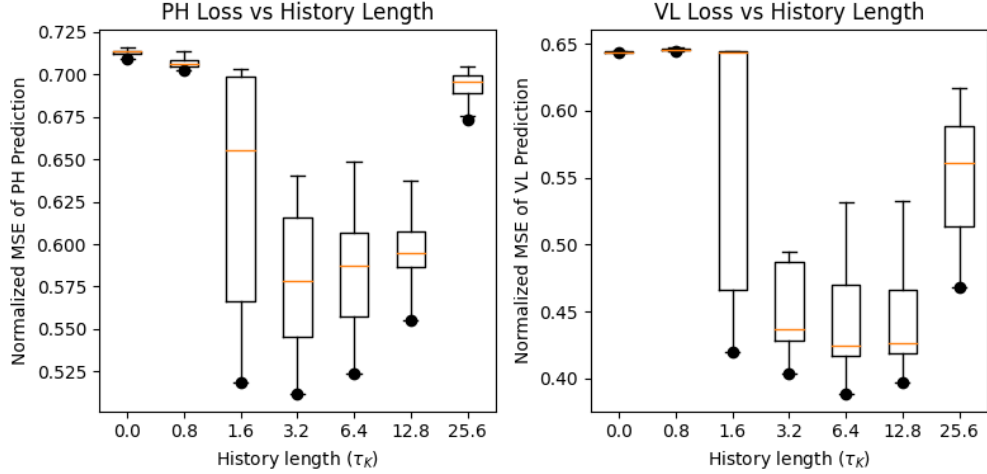


Figure 4: We show loss (normalized by loss using “no model” prediction) as a function of history length - TBNN is represented by zero history length. Results show clear benefit of including history in prediction - but also a diminishing return. Solid circles represent the best performing model in each case. The improvement is about 20% for the pressure Hessian, and nearly 40% for the viscous Laplacian. Samples for these distributions are taken from the hyperparameter search outlined in Section[3].

tests projected the predicted VGT ensemble into the topologically relevant Q - R phase plane, where

$$Q = -\frac{1}{2}\text{tr}(\mathbf{A}^2) \quad R = -\frac{1}{3}\text{tr}(\mathbf{A}^3). \quad (25)$$

Introduced by [10], the Q - R phase plane encodes the instantaneous and spatially infinitesimal topology of material deformation resulting from an observation of the VGT. Due to its interpretability and characterization of unique aspects of turbulent flow, the phase plane was used to explore and explain many phenomenology of the VGT in incompressible turbulence (see e.g. [3],[4],[7],[23]) as well as evaluate models’ predictive capability. A recent line of work [11],[12] has proposed a variation, the q - r phase plane, with

$$q = -\frac{1}{2}\text{tr} \left[\left(\frac{\mathbf{A}}{\|\mathbf{A}\|_2} \right)^2 \right] \quad r = -\frac{1}{3}\text{tr} \left[\left(\frac{\mathbf{A}}{\|\mathbf{A}\|_2} \right)^3 \right]. \quad (26)$$

The q - r phase plane is compact (a useful trait for model comparison under heavy-tailed statistics, which Lagrangian turbulence exhibits), and removes magnitude, allowing a richer topological picture to emerge [12]. Further, data analysis across a range of flow types and Reynolds numbers suggest a degree of universality[13].

Thus our *posteriori* tests consist of PDFs in the q, r phase plane, and distributions of longitudinal and transverse VGT components, highlighting intermittency. Comparisons of PDFs in Q - R were also performed, performance

Finally, we analyze the structure of the learned convolution kernels to extract statistical properties of the VGT history that are relevant for predicting the VL and PH terms.

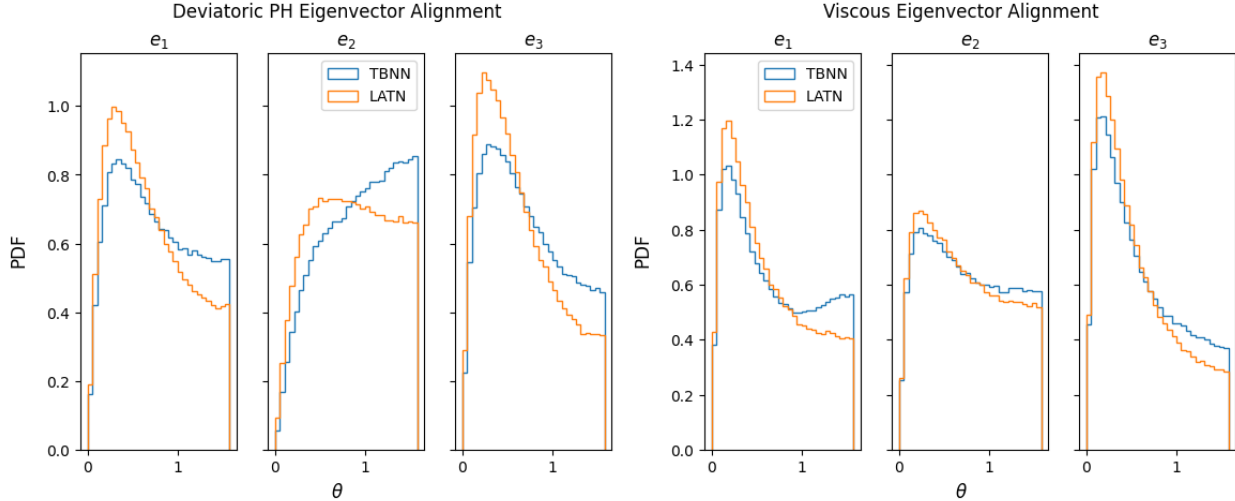


Figure 5: The LATN outperforms the TBNN in pressure Hessian and viscous Laplacian eigenvector alignment with the Ground Truth (DNS) – pick at the smaller values indicates better alignment. Here e_1 is the eigenvector with largest eigenvalue. For the viscous term, only the symmetric portion is considered.

4.1 *A Priori* Results

First, we note the unsurprising monotonic improvement in the *a-priori* measures, such as the test loss shown in Fig. (4) and the eigenvector alignment PDFs in Figs. (5, 6). The LATN incorporates strictly more information than the TBNN by leveraging the historical context of individual samples, allowing the g_θ 's to adapt accordingly. However, the magnitude of the improvement is remarkable—e.g., using the L_2 loss values, the LATN outperforms the TBNN by a percentage similar to the TBNN's improvement over a baseline “no model” scenario. These improvements in the *a-priori* metrics highlight the degree of degeneracy in the TBNN formulation, suggesting underutilized expressivity in its local-in-time tensor basis.

Observing the loss versus history length in Fig. (4), we find that memories of length $2-6\tau_K$ yield the best results. This observation supports and reinforces the phenomenological idea of limited memory, as diminishing returns are evident when including longer histories. From an information perspective, it is plausible that networks with extended memory lengths experience reduced signal-to-noise ratios as the VGT samples traverse varying flow topologies and intermittency. Regularizing the kernels via penalties in the loss function may help networks with long memories achieve comparable performance.

Turning to the eigenvector alignment PDFs, Fig. (5) illustrates the individual alignment of the predicted eigenvectors of the PH and VL with the ground truth for both the LATN and TBNN models. The PH predictions show a significant improvement, with the PDF sharply peaking at the optimal alignment $\theta = 0$ for the eigenvectors with the largest magnitudes (e_1 and e_3), and with a substantial increase in the probability of alignment for e_2 . Since the L_2 metric is used during training, alignment to e_1 or e_3 is expected, as these would contribute most to the loss. Improved alignment to e_2 , however, likely reflects simultaneous alignment of e_1 and e_3 .

To validate this interpretation, we present the joint PDF of the alignments θ_1

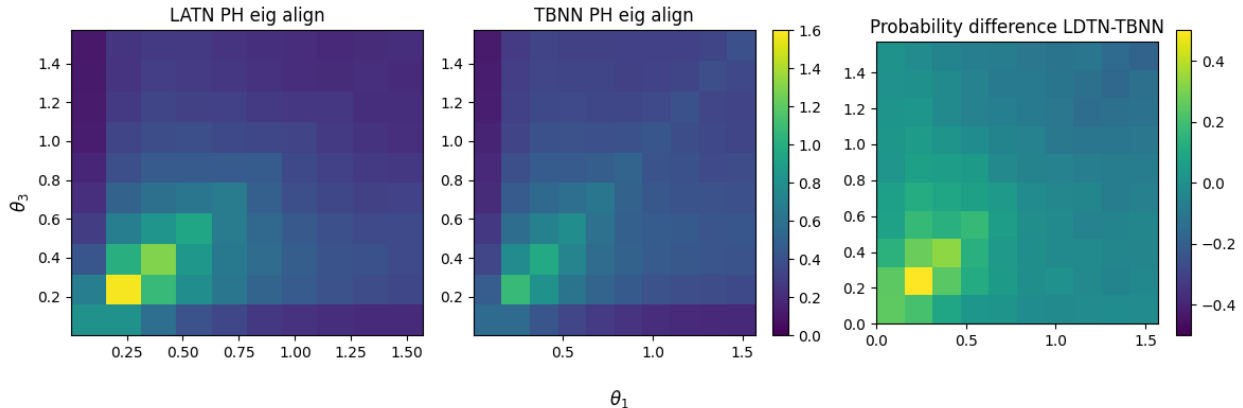


Figure 6: Joint PDF of the alignment θ_1, θ_3 . Following from Fig. (5), the ideal alignment is a delta function in the bottom-left corner. This figure shows that not only does LATN individually align e_1, e_3 better than the TBNN, but it simultaneously aligns the eigenvectors more often. Note that by aligning e_1, e_3 simultaneously, orthogonality ensures alignment of e_2 . Quantitatively, using the Earth-Mover Metric (EMM), LATN is a 10% improvement over TBNN when measuring with respect to the ideal distribution.

and θ_3 in Fig. (6). As seen clearly, the LATN exhibits a much stronger peak for simultaneous alignment and almost never misaligns both eigenvectors. Additionally, the simultaneous alignment of e_1 and e_3 implies improved alignment with e_2 due to the orthogonality of the eigenvectors.

In conclusion, the LATN demonstrates a remarkable ability to capture and predict the structure of the PH and VL terms, significantly outperforming the TBNN model.

4.2 *A-Posteriori* Results

The more stringent test is the (*physics*)-*a-posteriori* evaluation, as shown in Figs. (7-8). These figures present joint statistics after the respective models evolve a DNS initial condition over a large-eddy turnover time ($100\tau_K$). For this evaluation, we employ the normalized q - r phase plane proposed by [12], as its normalization and compact representation provide a clear visualization of topological prediction.

Fig. (7) illustrates that the LATN effectively resists the asymptotic pure-strain topologies often induced by Reynolds number effects (RE dynamics). Moreover, the LATN exhibits noticeable improvements over the TBNN prediction in most regions of the phase plane. However, the LATN is somewhat overly conservative, with much of the discrepancy between the LATN and DNS data arising from a concentration of topologies away from the extremes.

The VGT component PDFs in Fig. (8) demonstrate that the LATN closely matches the DNS distribution, deviating significantly only in the very low-probability extreme events. This long-term stability is attributed to the NODE training step, which effectively regularizes the model and enhances its robustness over extended evolutions.

To quantitatively compare multidimensional probability distributions, we employ the Earth Mover’s Distance (EMD). For completeness, this historical metric and its advantages in handling discrete probability distributions are detailed in Appendix 6.1.

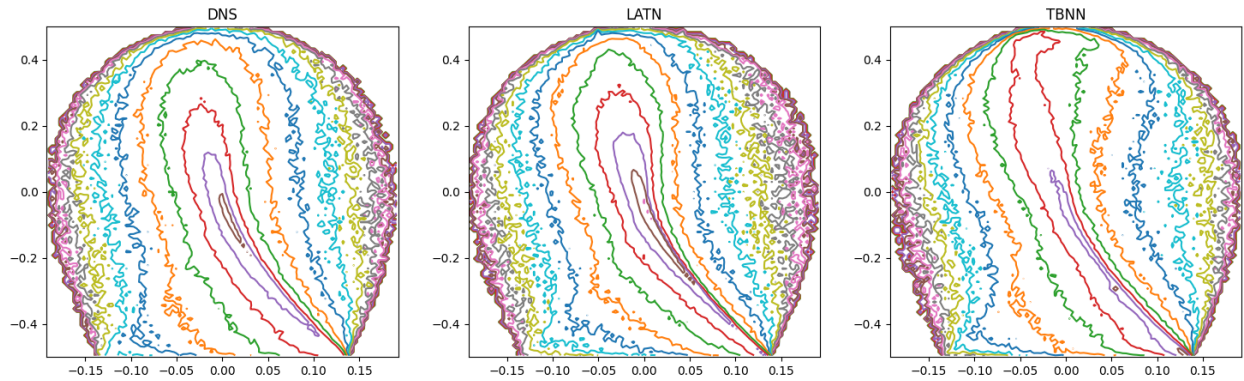


Figure 7: The statistics of VG topology in the normalized q - r phase plane. Here the improvement in prediction accuracy is more evident. The compact phase-plane removes bias of the magnitude of the VG, and shows clearly an improvement to the statistical topology. Quantitatively, LATN is 23% better match to DNS than TBNN.

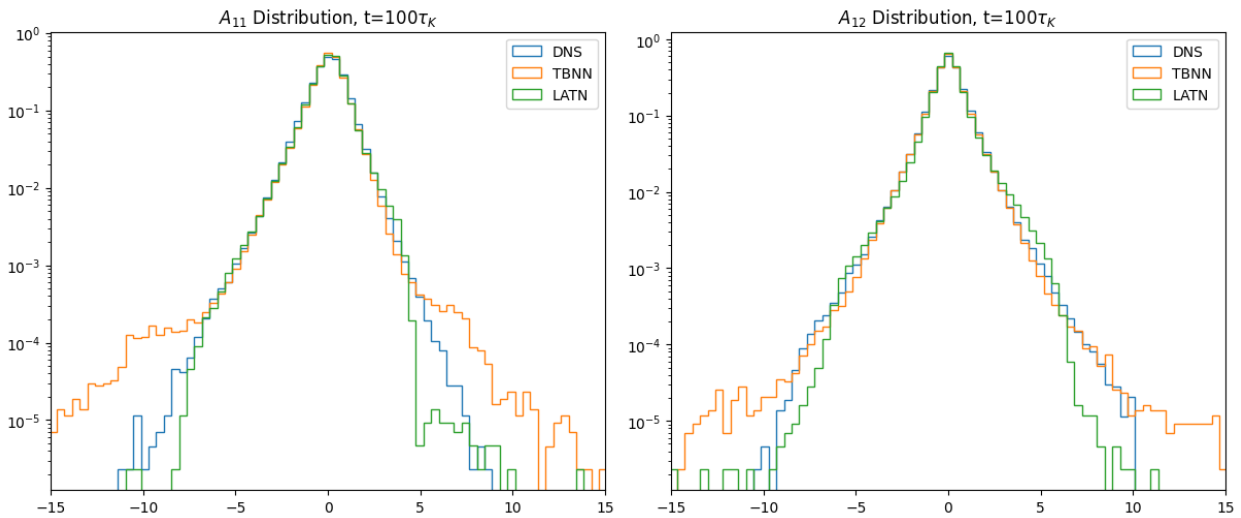


Figure 8: Distributions of $A_{11}^* := A_{11}/\sqrt{\langle A_{11}^2 \rangle}$ and $A_{12}^* := A_{12}/\sqrt{\langle A_{12}^2 \rangle}$ for DNS, LATN, and TBNN. The log scale emphasizes discrepancies in the tails of the distributions.

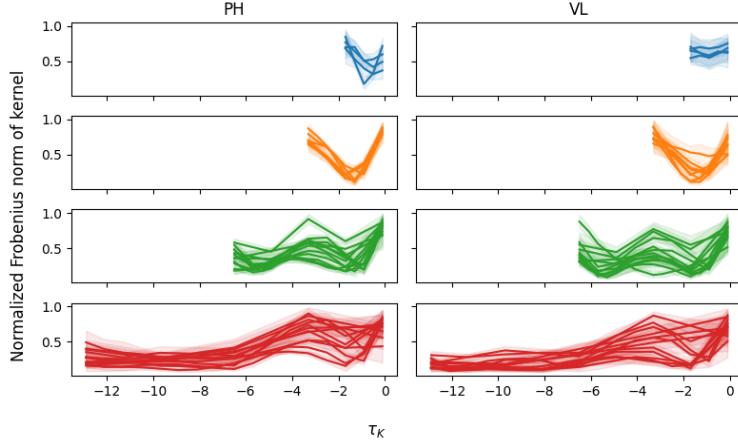


Figure 9: Learned time kernel norms per kernel length. The mean is shown in solid, while a 2σ band is shaded. The magnitude of the norms remain significant, up to $\sim 8\tau_K$. The oscillatory nature of the kernels likely points to redundancy in the timeseries data. Kernel training was not regularized, thus the tendencies shown are purely those the network found most informative. Each curve is a particular choice of hyper-parameters, and the mean and variance are calculated across filters per trained model.

Applying the EMD to the *a-posteriori* distributions, we observe that the LATN achieves improvements of 10% and 23% in *a priori* PH eigenvector alignment (Fig. (6)), and *a-posteriori* *q-r* PDF prediction (Fig. (7)) respectively.

These improvements highlight the enhanced accuracy of the LDTN across multiple metrics and its ability to approximate the underlying dynamics effectively.

4.3 Interpreting Memory Kernels

Turning to the interpretation of the convolutional kernels, we identify two intriguing properties: learned symmetry and rate of decay. First, the best-performing models exhibit a high degree of symmetry in the learned kernels. To quantify this, we define a symmetry metric for a matrix \mathbf{M} as:

$$sym(\mathbf{M}) = \frac{\|\mathbf{S}_M\| - \|\mathbf{A}_M\|}{\|\mathbf{S}_M\| + \|\mathbf{A}_M\|}, \quad \text{where } \mathbf{S}_M \doteq \frac{1}{2}(\mathbf{M} + \mathbf{M}^T), \quad \mathbf{A}_M \doteq \frac{1}{2}(\mathbf{M} - \mathbf{M}^T). \quad (27)$$

Here, if \mathbf{M} is symmetric, $\mathbf{A}_M = 0$, resulting in $sym(\mathbf{M}) = 1$, while if \mathbf{M} is skew-symmetric, $sym(\mathbf{M}) = -1$.

Fig. 10 shows the probability distribution of $sym(\mathbf{K})$, where \mathbf{K} are convolutional kernels aggregated over history and filter number, as well as across various neural network hyperparameter configurations. The distributions are shown at initialization and after tangent-space training for the PH and VL terms. For the PH prediction, the kernels demonstrate a strong preference for symmetry, with the first moments of the symmetry distributions quantified in Table 1.

Focusing on a single timestep in the convolution, i.e., fixing m and ℓ in $\mathbf{K} \doteq K_{ij}^{(m,\ell)}$, suppose the kernel is symmetric, $\mathbf{K} = \mathbf{K}^T$. For a sample of the VGT \mathbf{A} , with

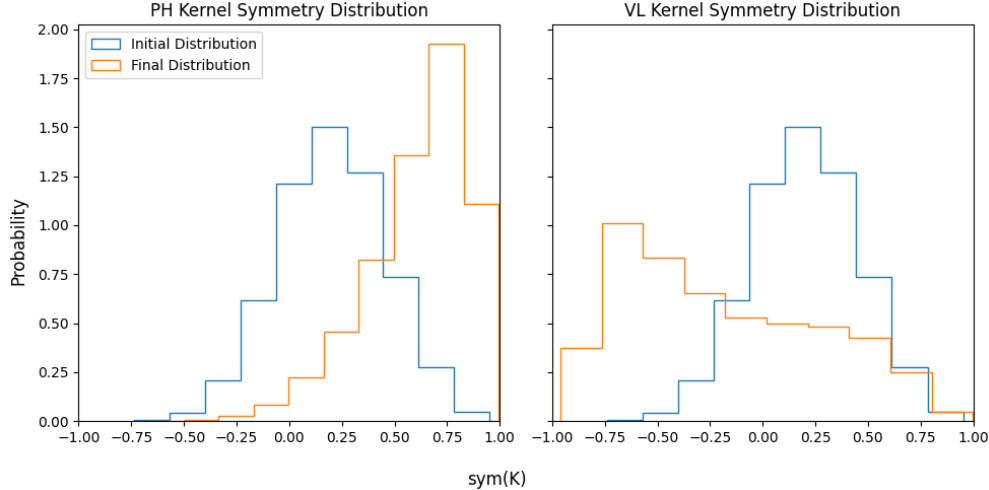


Figure 10: Measurements of learned kernel symmetry. Blue outline shows the distribution that the initial parameters were pulled from, while orange shows a histogram of the learned kernels for the (left) pressure Hessian and (right) viscous Laplacian LDTNs. The kernels are aggregated over filter, time, and hyperparameter search. We observe that while we provide no steering of these kernel structures, the kernels in the PH network tend to be very symmetric, while the VL does not appear to have a structural preference. The PH result suggests inclusion of the history of the strain-rate tensor is driving the improvement in performance. Moments of these distributions are listed in Table 1.

corresponding strain-rate and rotation-rate tensors \mathbf{S} and \mathbf{W} , respectively, we have:

$$\mathbf{K} \odot \mathbf{A} = \mathbf{K} \odot (\mathbf{S} + \mathbf{W}) = \mathbf{K} \odot \mathbf{S} + \mathbf{K} \odot \mathbf{W} = \mathbf{K} \odot \mathbf{S}, \quad (28)$$

where \odot denotes element-wise multiplication. This shows that in predicting the pressure Hessian, the network primarily focuses on the time-history of the strain-rate tensor.

The results for the VL are less clear. While asymmetric kernels are indeed learned, the preference for asymmetry is not as pronounced, as illustrated by the large variance in Table 1. This lack of clarity may be attributed to the slight symmetry present in the kernel initialization, leaving the results inconclusive.

| kernel distribution | mean($sym(K)$) | std($sym(K)$) |
|---------------------|------------------|-----------------|
| random | 0.206 | 0.249 |
| trained ph | 0.611 | 0.239 |
| trained vl | -0.188 | 0.464 |

Table 1: First and second moments of symmetry metric distributions applied to the random (pre-training) and post-training memory kernels. While the change in the mean distribution is of near-equal magnitude for the PH and VL histories, the PH retains a much tighter distribution (lower variance) centered at a higher symmetry.

5 Conclusion

In this work, we introduced and evaluated the Lagrangian Attention Tensor Network (LATN), a novel fusion of phenomenological deformation theory and data-driven modeling. The LATN demonstrated state-of-the-art predictive capabilities in both *a-priori* and *a-posteriori* metrics, significantly outperforming the previous best Tensor Basis Neural Network (TBNN).

By employing an interpretable, physics-informed and transformer architecture based (auto-regressive memory) machine learning structure, we were able to deduce (at least partially) the source of these improvements: namely, the ability to observe and leverage time correlations in the strain-rate tensor over timescales of approximately $5-10\tau_K$.

While this work suggests promising directions in both phenomenology and data-driven modeling, several potential avenues for improvement remain:

- **Generalizing to continuous time:** The current modeling relies on a fixed, small simulation timestep $\Delta t = \tau_K/10$. This not only incurs unnecessary computational cost for slow-evolving regions of the flow but also restricts the kernels to a particular temporal resolution. Extending the approach to continuous time is a challenging but fundamental step toward a more robust and complete solution.
- **Kernel regularization:** Currently, we rely solely on the information content of the data to encourage kernel decay. Introducing explicit regularization strategies could help sparsify the learned kernels where appropriate, reducing overfitting and enhancing interpretability.
- **Phenomenological insights:** Further investigation into the structure of the learned kernels may reveal valuable insights into the correlations that the LATN identifies as critical for predicting the pressure Hessian (PH) and viscous Laplacian (VL). Such insights could lead to theoretical advances and improved models.
- **Faithful statistical reproduction:** Recent works (e.g., [5],[14]) targeted the reproduction of turbulent stationary statistics from the outset. An exciting open avenue is the integration of our physics-informed, autoregressive model into these frameworks. This would yield a model trajectory-accurate at timescales sub-Kolmogorov, while respecting stationary statistics. One avenue towards this goal could involve allowing the stochastic forcing to depend on the VGT, i.e., modifying $\mathbf{F}(D_s, D_a)$ to $\mathbf{F}(D_s(A), D_a(A))$. This adaptation could equitably distribute forcing and help drive trajectories away from concentration points, improving the alignment with DNS stationary statistics.

By addressing these directions, future work can refine the LATN framework, enhancing its applicability and theoretical grounding while continuing to bridge the gap between phenomenology and data-driven approaches.

6 Appendix

6.1 Earth Mover Metric

To quantitatively compare multi-dimensional probability distributions, we utilize the Earth Mover’s Distance (EMD) [33, 38, 39]. For discrete probability distributions

$P, Q : \Omega \rightarrow \mathbb{R}$, parameterized by p, q , the EMD is defined as:

$$\begin{aligned} emd(P, Q) &:= \min_f \sum_{p \in P} \sum_{q \in Q} c_{pq} f_{pq} \\ \text{subject to: } & f_{pq} \geq 0, \quad \sum_{p \in P} f_{pq} = y_q, \quad \sum_{q \in Q} f_{pq} \leq x_p. \end{aligned}$$

This metric has numerous qualitative advantages over commonly used alternatives such as the Kullback-Leibler divergence, particularly for multi-dimensional discrete distributions. As demonstrated in its application to image retrieval [38], the EMD offers symmetry and explicitly incorporates the underlying metric via c_{pq} . This flexibility allows us to inherit the metric from Ω and enables a more meaningful comparison of distributions under this metric.

Interpreting $emd(P, Q)$ as the amount of work required to transform P into Q , we define a relative measure of improvement:

$$remd_{\mathcal{I}}(P, Q) := 1 - \frac{emd(\mathcal{I}, P)}{emd(\mathcal{I}, Q)},$$

where \mathcal{I} represents an “ideal” distribution, which will be specified in the relevant context. The value $remd_{\mathcal{I}}(P, Q)$ represents the percentage improvement of P over Q relative to \mathcal{I} . It immediately follows that:

$$remd_{\mathcal{I}}(P, Q) > 0 \iff emd(P, \mathcal{I}) < emd(Q, \mathcal{I}).$$

References

- [1] Wm. T. Ashurst, A. R. Kerstein, R. M. Kerr, and C. H. Gibson. Alignment of vorticity and scalar gradient with strain rate in simulated navier–stokes turbulence. *The Physics of Fluids*, 30(8):2343–2353, 1987.
- [2] Dhawal Buaria and Katepalli R. Sreenivasan. Forecasting small-scale dynamics of fluid turbulence using deep neural networks. *Proceedings of the National Academy of Sciences*, 120(30), July 2023.
- [3] Brian J. Cantwell. Exact solution of a restricted euler equation for the velocity gradient tensor. *Physics of Fluids A: Fluid Dynamics*, 4(4):782–793, 1992.
- [4] Brian J Cantwell. On the behavior of velocity gradient tensor invariants in direct numerical simulations of turbulence. *Physics of Fluids A: Fluid Dynamics*, 5(8):2008–2013, 1993.
- [5] Maurizio Carbone, Vincent J Peterhans, Alexander S Ecker, and Michael Wilczek. Tailor-designed models for the turbulent velocity gradient through normalizing flow. *arXiv preprint arXiv:2402.19158*, 2024.
- [6] Tian Qi Chen, Yulia Rubanova, Jesse Bettencourt, and David Duvenaud. Neural ordinary differential equations. *CoRR*, abs/1806.07366, 2018.
- [7] Michael Chertkov, Alain Pumir, and Boris I. Shraiman. Lagrangian tetrad dynamics and the phenomenology of turbulence. *Physics of Fluids*, 11(8):2394–2410, 1999.

- [8] Michael (Misha) Chertkov. Mixing artificial and natural intelligence: From statistical mechanics to ai and back to turbulence. *Journal of Physics A: Mathematical and Theoretical*, 57(33):333001, 2024.
- [9] Laurent Chevillard and Charles Meneveau. Lagrangian dynamics and statistical geometric structure of turbulence. *Physical review letters*, 97(17):174501, 2006.
- [10] M. S. Chong, A. E. Perry, and B. J. Cantwell. A general classification of three-dimensional flow fields. *Physics of Fluids A: Fluid Dynamics*, 2(5):765–777, 1990.
- [11] Rishita Das and Sharath S. Girimaji. On the reynolds number dependence of velocity-gradient structure and dynamics. *Journal of Fluid Mechanics*, 861:163–179, 2019.
- [12] Rishita Das and Sharath S. Girimaji. Characterization of velocity-gradient dynamics in incompressible turbulence using local streamline geometry. *Journal of Fluid Mechanics*, 895:A5, 2020.
- [13] Rishita Das and Sharath S Girimaji. The effect of large-scale forcing on small-scale dynamics of incompressible turbulence. *Journal of Fluid Mechanics*, 941:A34, 2022.
- [14] Rishita Das and Sharath S. Girimaji. Data-driven model for Lagrangian evolution of velocity gradients in incompressible turbulent flows, 2023. [eprint: 2304.14529](#).
- [15] K. Duraisamy, G. Iaccarino, and H. Xiao. Turbulence modeling in the age of data. *Annual Review of Fluid Mechanics*, 51:357, 2019.
- [16] G. Falkovich, K. Gawedzki, and M. Vergassola. Particles and fields in fluid turbulence. *Rev. Mod. Phys.*, 73:913–975, Nov 2001.
- [17] Uriel Frisch. *Turbulence: The Legacy of A. N. Kolmogorov*. Cambridge University Press, 1995.
- [18] SS Girimaji and SB Pope. A diffusion model for velocity gradients in turbulence. *Physics of Fluids A: Fluid Dynamics*, 2(2):242–256, 1990.
- [19] Criston Hyett, Yifeng Tian, Michael Woodward, Michael Chertkov, Daniel Livescu, and Mikhail Stepanov. Applicability of machine learning methodologies to model the statistical evolution of the coarse-grained velocity gradient tensor. *Bulletin of the American Physical Society*, 2022.
- [20] Eunhwan Jeong and Sharath S Girimaji. Velocity-gradient dynamics in turbulence: effect of viscosity and forcing. *Theoretical and computational fluid dynamics*, 16(6):421–432, 2003.
- [21] Javier Jimenez and Robert D Moser. Large-eddy simulations: where are we and what can we expect? *AIAA journal*, 38(4):605–612, 2000.
- [22] Perry L. Johnson and Charles Meneveau. A closure for lagrangian velocity gradient evolution in turbulence using recent-deformation mapping of initially gaussian fields. *Journal of Fluid Mechanics*, 804:387–419, 2016.
- [23] Perry L. Johnson and Michael Wilczek. Multiscale Velocity Gradients in Turbulence. *Annual Review of Fluid Mechanics*, 56(1):annurev-fluid-121021-031431, January 2024.

- [24] Ryan King, Oliver Hennigh, Arvind Mohan, and Michael Chertkov. From Deep to Physics-Informed Learning of Turbulence: Diagnostics, December 2018. arXiv:1810.07785 [nlin, physics:physics, stat].
- [25] A. N. Kolmogorov. The local structure of turbulence in incompressible viscous fluid for very large reynolds numbers. *First published in Russian in Dokl. Akad. Nauk SSSR (1941) 30(4). Reprinted in English in Proceedings of the Royal Society of London. Series A: Mathematical and Physical Sciences*, 434(1890):9–13, 1991.
- [26] J.M. Lawson and J.R. Dawson. On velocity gradient dynamics and turbulent structure. *Journal of Fluid Mechanics*, 780:60–98, 2015.
- [27] Yi Li and Charles Meneveau. Material deformation in a restricted euler model for turbulent flows: analytic solution and numerical tests. *Physics of Fluids*, 19(1), 2007.
- [28] Julia Ling, Andrew Kurzawski, and Jeremy Templeton. Reynolds averaged turbulence modelling using deep neural networks with embedded invariance. *Journal of Fluid Mechanics*, 807:155–166, November 2016.
- [29] Jesús Martín, César Dopazo, and Luis Valiño. Dynamics of velocity gradient invariants in turbulence: restricted euler and linear diffusion models. *Physics of Fluids*, 10(8):2012–2025, 1998.
- [30] R. Maulik, O. San, A. Rasheed, and P. Vedula. Subgrid modelling for two-dimensional turbulence using neural networks. *Journal of Fluid Mechanics*, 858:122, 2019.
- [31] Charles Meneveau. Lagrangian dynamics and models of the velocity gradient tensor in turbulent flows. *Annual Review of Fluid Mechanics*, 43:219–245, 2011.
- [32] Arvind T. Mohan, Nicholas Lubbers, Misha Chertkov, and Daniel Livescu. Embedding hard physical constraints in neural network coarse-graining of three-dimensional turbulence. *Physical Review Fluids*, 8(1):014604, January 2023.
- [33] Gaspard Monge. Mémoire sur la théorie des déblais et des remblais. *Mem. Math. Phys. Acad. Royale Sci.*, pages 666–704, 1781.
- [34] Koji Ohkitani and Seigo Kishiba. Nonlocal nature of vortex stretching in an inviscid fluid. *Physics of Fluids*, 7(2):411–421, 1995.
- [35] Nishant Parashar, Balaji Srinivasan, and Sawan S Sinha. Modeling the pressure-hessian tensor using deep neural networks. *Physical Review Fluids*, 5(11):114604, 2020.
- [36] S. B. Pope. A more general effective-viscosity hypothesis. *Journal of Fluid Mechanics*, 72(2):331–340, 1975.
- [37] G. D. Portwood, P. P. Mitra, M. D. Ribeiro, T. M. Nguyen, B. T. Nadiga, J. A. Saenz, M. Chertkov, A. Garg, A. Anandkumar, A. Dengel, and others. Turbulence forecasting via neural ode. *arXiv preprint arXiv:1911.05180*, 2019.
- [38] Yossi Rubner, Carlo Tomasi, and Leonidas J Guibas. A metric for distributions with applications to image databases. In *Sixth international conference on computer vision (IEEE Cat. No. 98CH36271)*, pages 59–66. IEEE, 1998.
- [39] Yossi Rubner, Carlo Tomasi, and Leonidas J Guibas. The earth mover’s distance as a metric for image retrieval. *International journal of computer vision*, 40:99–121, 2000.

- [40] Maurits H Silvis, Ronald A Remmerswaal, and Roel Verstappen. Physical consistency of subgrid-scale models for large-eddy simulation of incompressible turbulent flows. *Physics of Fluids*, 29(1), 2017.
- [41] A. J. M. Spencer and R. S. Rivlin. Further results in the theory of matrix polynomials. *Arch. Rational Mech. Anal.*, 4:214–230, 1959.
- [42] Yifeng Tian, Yen Ting Lin, Marian Anghel, and Daniel Livescu. Data-driven learning of mori–zwanzig operators for isotropic turbulence. *Physics of Fluids*, 33(12):125118, 2021.
- [43] Yifeng Tian, Daniel Livescu, and Michael Chertkov. Physics-informed machine learning of the lagrangian dynamics of velocity gradient tensor. *Physical Review Fluids*, 6(9):094607, 2021.
- [44] Yifeng Tian, Michael Woodward, Mikhail Stepanov, Chris Fryer, Criston Hyett, Daniel Livescu, and Michael Chertkov. Lagrangian large eddy simulations via physics-informed machine learning. *Proceedings of the National Academy of Sciences*, 120(34):e2213638120, August 2023.
- [45] A. Tsinober, E. Kit, and T. Dracos. Experimental investigation of the field of velocity gradients in turbulent flows. *J. Fluid Mech.*, 242:169–192, 1992.
- [46] A Vaswani. Attention is all you need. *Advances in Neural Information Processing Systems*, 2017.
- [47] P. Vieillefosse. Internal motion of a small element of fluid in an inviscid flow. *Physica A*, 125:150–162, 1984.
- [48] P. Vieillefosse. Internal motion of a small element of fluid in an inviscid flow. *Physica A: Statistical Mechanics and its Applications*, 125(1):150–162, 1984.
- [49] Dimitar G Vlaykov and Michael Wilczek. On the small-scale structure of turbulence and its impact on the pressure field. *Journal of Fluid Mechanics*, 861:422–446, 2019.
- [50] A. Waibel, T. Hanazawa, G. Hinton, K. Shikano, and K.J. Lang. Phoneme recognition using time-delay neural networks. *IEEE Transactions on Acoustics, Speech, and Signal Processing*, 37(3):328–339, 1989.
- [51] M Wan, S Chen, G Eyink, C Meneveau, E Perlman, R Burns, Y Li, A Szalay, and S Hamilton. Johns hopkins turbulence database (jhtdb), 2016.
- [52] J.-X. Wang, J.-L. Wu, and H. Xiao. Physics-informed machine learning approach for reconstructing reynolds stress modeling discrepancies based on dns data. *Physical Review Fluids*, 2:034603, 2017.
- [53] Michael Woodward, Yifeng Tian, Criston Hyett, Chris Fryer, Mikhail Stepanov, Daniel Livescu, and Michael Chertkov. Physics-informed machine learning with smoothed particle hydrodynamics: Hierarchy of reduced Lagrangian models of turbulence. *Physical Review Fluids*, 8(5):054602, May 2023.
- [54] Haitao Xu, Alain Pumir, and Eberhard Bodenschatz. The pirouette effect in turbulent flows. *Nature Physics*, 7(9):709–712, 2011.
- [55] Q.-S. Zheng. On the representations for isotropic vector-valued, symmetric tensor-valued and skew-symmetric tensor-valued functions. *International Journal of Engineering Science*, 31(7):1013–1024, 1993.